FOREX Publication
Open Access | Rapid and quality publishing

International Journal of
Electrical and Electronics Research (IJEER)
Research Article | Volume 14, Issue 2 | Pages 467-478 | e-ISSN: 2347-470X

A Learned Three Operator Splitting Network for Accelerated MRI Reconstruction Using Complex-Valued Deep Unrolling

David Muigai[1*], Elijah Mwangi[2], and Henry Kiragu[3]

[1]Department of Electrical Engineering, Pan African University Institute of Basic Sciences, Technology and Innovation, Nairobi, Kenya; Email: david.waweru@egerton.ac.ke
[2]Faculty of Engineering, University of Nairobi, Kenya; Email: elijah.mwangi@uonbi.ac.ke
[3]Department of Electrical and Telecommunication Engineering, Multimedia University of Kenya, Nairobi, Kenya; Email: hkiragu@mmu.ac.ke

***Correspondence:** *David Muigai; david.waweru@egerton.ac.ke*

ABSTRACT- Magnetic Resonance Imaging (MRI) is the cornerstone of modern medical diagnosis and research, providing high spatial resolution visualization of the anatomical and functional information of the body's internal structure in a non-ionizing, non-carcinogenic and non-invasive manner. Despite these superior properties, the MRI data acquisition process is inherently slow, limiting this technique in scenarios where time is crucial. Consequently, accelerating MRI through k-space under-sampling at sub-Nyquist rates and reconstructing high-quality images from incomplete measurements has emerged as an active area of research in the past few decades. This paper proposes a learned three-operator splitting algorithm implemented in an unrolled complex-valued deep neural network architecture for accelerated Magnetic Resonance (MR) image reconstruction. Objective results evaluated using Peak Signal–to–Noise Ratio (PSNR), Structural Similarity Index (SSIM) and Normalized Root–Mean–Squared Error (NRMSE) at ×2 to ×5 acceleration show superior reconstruction performance of the proposed network compared to other state–of–the–art learned algorithms at comparable reconstruction time. Subjective results show that the proposed network reconstructed images visually similar to ground truth images. The proposed network has the potential to enable real-time MRI applications with high-quality images.

Keywords: Accelerated MRI Reconstruction, Compressed Sensing, Complex-Valued Deep Learning, Learned Three Three-Operator Splitting Network.

ARTICLE INFORMATION
Author(s): David Muigai, Elijah Mwangi, Henry Kiragu;
Received: 05/03/26; **Accepted**: 17/05/26; **Published**: 30/06/26;
E- ISSN: 2347-470X;
Paper Id: IJEER 0503B03;
Citation: 10.37391/ijeer.140223
Webpage-link:
https://ijeer.forexjournal.co.in/archive/volume-14/ijeer-140223.html

1. INTRODUCTION

Magnetic resonance imaging (MRI) is a vital diagnostic and research tool in medicine, providing detailed visualization of the human anatomy with excellent soft tissue contrast and spatial resolution in a non-carcinogenic, non-ionizing and non-invasive manner. Due to these properties, the MRI technique has found numerous applications in clinical examinations and research, ranging from lesion detection to investigating the functionality of critical body organs [1]. Unfortunately, the MRI data acquisition process is inherently slow, with current procedures ranging from 30 minutes to 2 hours. This long scan time is disadvantageous as it limits access to MRI, leading to patients waiting for longer times for appointments and potentially delaying diagnosis and treatment. Some patients experience claustrophobic discomfort, and it can also introduce motion–related artifacts in generated images.

The MRI data is collected by superposing a magnetic spin with a static magnetic field and measuring the generated signal as a function of frequency and phase. Therefore, the MRI signal is measured in the Fourier domain or the k-space, and is complex in nature. The image can be obtained by an inverse Fourier Transform; however, filling the entire k-space is a time-consuming process. This has made reconstructing Magnetic Resonance (MR) images from data collected at sub-Nyquist rates a primary research focus in MRI acceleration [2, 3, 4, 5]. These sub-Nyquist rates violate the Shannon-Nyquist sampling theorem, and an inverse Fourier Transform of the under sampled k-space results in a heavily aliased reconstructed image with low Signal-to-Noise Ratio (SNR) and severe imaging artifacts.

Compressed Sensing (CS) methods [6, 7, 8, 9] enable image reconstruction from under sampled k-space data by formulating an optimization problem that incorporates prior knowledge of the image, such as smoothness and sparsity in some transform or spatial domain, to regularize the solution. However, these classical CS reconstruction methods face three major limitations. First, these methods rely on iterative optimization procedures that result in slow reconstruction times. Second, the regularization functions and their hyperparameters are non-trivial and highly problem-specific, making it difficult to choose

FOREX Publication
Open Access | Rapid and quality publishing
International Journal of Electrical and Electronics Research (IJEER)
Research Article | Volume 14, Issue 2 | Pages 467-478 | e-ISSN: 2347-470X

to achieve optimal performance, limited generalization and poor applicability. Finally, at high acceleration factors, these methods tend to produce residual aliasing artifacts [10], which can reduce the diagnostic reliability of the reconstructed image.

Recently, Deep Learning (DL) approaches [11, 12, 13] have yielded superior results in terms of reconstruction quality and speed compared to classical algorithms. In contrast to conventional CS methods, the DL approaches implicitly learn prior information and regularization directly from data, eliminating the need to explicitly define them within the training objective. These approaches employ deep neural networks for learning, enabling a fast and efficient reconstruction that can be readily applied to newly acquired data. The DL approaches can be broadly classified into two categories, namely end-to-end learning and deep unfolding methods. The DL methods that involve end-to-end learning [13, 14, 15, 16, 17] map noisy, artifact-contaminated k-space or image into high-quality images or k-space. This effectively reduces artifacts and enhances image clarity and resolution. The performance of these methods is largely dictated by the network architecture, often having limited interpretability due to the absence of explicit guidance from the underlying imaging model. Therefore, these methods have reduced transparency and may struggle to achieve optimal reconstruction.

Deep Unrolling Networks (DUN) [3, 18, 19, 20, 21, 22, 23] overcome the aforementioned limitations of classical CS and end-to-end DL methods by integrating their complementary strengths—namely, the physical interpretability of the former and the powerful data-driven prior learning capability of the latter. The networks unroll the iterative procedures of optimization algorithms into a sequence of iterative modules stacked together to construct a supervised deep learning framework. The parameters of the original optimization algorithm are then learned adaptively through end-to-end training. Reconstructing MR images with deep unrolled networks typically decomposes the task into two components: a prior learning term and a data fidelity term. These algorithms incorporate both learnable and non-learnable data consistency layers, which are integrated within the data fidelity term to constrain the reconstruction process in the sampled regions of k-space, thereby substantially enhancing overall reconstruction quality. Nevertheless, most DUNs either operate on the magnitude of the k-space or the undersampled image or process the real and imaginary components as separate channels, which have potential limitations when dealing with significant phase variations. To address the aforementioned limitations in MRI reconstruction, we propose a learned three-operator splitting network (TOSNet) with the following specific contributions.

- We propose a learned reconstruction architecture inspired by the iterative three-operator splitting algorithm for MRI reconstruction with learned hyperparameters.
- We employ complex-valued convolutional neural network and complex-valued U-Net in learning the regularization yielding TOSNet and TOSNet^{+} respectively. This alleviates potential limitations when significant phase variations occur and offer richer representation in MRI.
- We conducted extensive experiments on two publicly available raw k-space datasets namely, FastMRI and the Open access multi-coil K-space dataset for Cardiovascular Magnetic Resonance imaging (OCMR) to demonstrate the superior performance of proposed networks and compare it with other existing state–of–the–art learned networks.

2. RELATED WORKS

In recent years, DUNs have shown great potential in accelerating MRI. Schlemper *et al.* [24] introduced a deep cascade of Convolutional Neural Networks (CNN) interleaved with data consistency layers to reconstruct dynamic two-dimensional (2D) cardiac magnetic resonance images from undersampled k-space. The authors also added a data sharing layer to exploit spatio-temporal correlations between frames. The network was trained on cardiac cine MRI data using Cartesian undersampling patterns. Experimental results evaluated using Peak Signal–to–Noise Ratio (PSNR) showed that the approach yielded superior image quality at a faster inference compared to several state of the art low - rank and CS methods. The method also preserves anatomical details effectively and outperforms traditional methods in perceptual quality. However, the approach relied on a relatively small dataset consisting of 10 subjects, each consisting of 30 temporal frames, giving a total of 300 images which can limit generalization. The approach also has a high computational and memory requirement, limiting its scalability to large datasets.

Duan *et al.* [25] introduced a deep learning framework called Variable Splitting Network (VS-Net) to accelerate parallel MRI by efficiently reconstructing multi-coil MR images from undersampled k-space. The network was obtained by unrolling the variable splitting optimization into a deep network architecture comprising three blocks in each unrolled iteration, namely the data consistency block, which uses analytical solutions to ensure consistency with acquired measurements, the denoiser block consisting of a CNN and a weighted average block for merging the denoiser and data consistency block. The network was trained and tested using a multicoil knee MRI dataset using 4× and 6× acceleration factors and evaluated using PSNR and Structural Similarity Index (SSIM). The VS-Net yielded higher PSNR values and comparable SSIM values compared to variational networks and the iterative ℓ_1- SPIRit methods. The main limitation of the network was reliance on a relatively small dataset comprising 20 subjects.

Fuin *et al.* [10] learned a Multi–Scale Variational Neural Network (MS-VNN) to accelerate reconstruction of free breathing motion compensated whole – heart 3-dimensional Coronary Magnetic Resonance Angiography (CMRA) from undersampled data. The MS-VNN learned two sets of activation functions and kernels for the magnitude and phase images of the complex-valued CMRA data. The network was trained on 10 blocks processing the complex data using separate phase and magnitude paths, while learned filters of multi-scale captured the small coronary structures. The MS-VNN reduced the acquisition and reconstruction time of CMRA compared to full sampling. The network outperformed the conventional VNN and wavelet-based CS in image quality, evaluated using

FOREX Publication
Open Access | Rapid and quality publishing
International Journal of Electrical and Electronics Research (IJEER)
Research Article | Volume 14, Issue 2 | Pages 467-478 | e-ISSN: 2347-470X

coronary artery sharpness and vessel length. The main limitation of the method was the relatively small training and evaluation data comprising 10 subjects which can limit generalization. The network was also tested on 10 independent subjects comprising 9 healthy volunteers and 1 patient with coronary artery disease. The MS-VNN relied on 2D translational motion correction and had a long offline training time of about 76 hours compared to the single-scale VNN with about 16 hours.

Xin *et al.* [26] presented a learned Half Quadratic Splitting Algorithm (HQS), which employed deep learning techniques to solve the regularization term while computing the data consistency term. The approach replaced the regulation term with a parametrized CNN learned from data, creating an unrolled network architecture to reconstruct MR images from undersampled data. The network consisted of 10 reconstruction blocks corresponding to 10 iterations of the HQS algorithm. The input data was a magnitude-zero-filled image normalized to [0, 1] and trained with a compound loss of ℓ_1 and Multi-Scale –SSIM. Qualitative results evaluated using PSNR, Normalized Root–Mean–Squared Error (NRMSE) and SSIM on Open access multi-coil k-space dataset for Cardiovascular MR (OCMR) showed superior results compared to other existing networks. Qualitative results show the network removed the undersampling artifacts and is similar to the ground truth image. However, differences between the reconstructed image and the ground truth can be seen using error maps and zoomed areas.

Fabian *et al.* [27] proposed a Hybrid Unrolled Multi-Scale architecture dubbed HUMUS-Net that merged transformers and CNNs to accelerate MR images reconstruction. The HUMUS-Net utilized the ability of transformers to capture long-range dependencies through self-attention and CNNs' ability to extract the local features efficiently in reconstructing MR images. This enabled the network to perform multi-scale feature extraction by processing low-resolution features using a transformer and high-resolution features using convolutions. The HUMUS-net incorporated a sensitivity map estimator for multi–coil MRI reconstruction and employed unrolled iterative reconstruction steps inspired by iterative optimization algorithms. The unrolled network achieved state – of – the – art results evaluated using SSIM, PSNR, and Normalized Mean Squared Error (NMSE), surpassing other existing networks. However, the HUMUS-net is computationally expensive and demands large memory, particularly from the transformer, restricting the network depth and patch size. The network also requires inputs of fixed size, limiting its flexibility in clinical applications.

Lian *et al*. [1] extended the HQS unfolding network by adding a learnable spatial–frequency difference aware module which maps the k-space differences to the image differences for perceptual compensation. The approach also decomposed the images into residual components and mean to introduce explicit priors. The approach solves the limitation of existing HQS algorithms, which lack specialized modules to learn the distribution of undersampling artifacts in the image domain. The architecture was tested using two datasets, namely FastMRI and Calgary-Campinas, and showed superior performance compared to other existing methods evaluated in terms of PSNR, SSIM and NMSE. However, the superior performance is achieved with higher computational cost compared to other existing methods. This resulted in longer training times, presenting challenges for practical deployment, especially in clinical settings with high turnarounds. Another challenge is the representation of the k-space, which is inherently complex. The approach treated the real and imaginary parts as separate channels, which may have limitations when significant phase variation occurs during reconstruction.

Zhang *et al.* [22] presented a Deep Unrolling Shrinkage Network (DUS-Net) that unrolled the Alternating Direction Method of Multipliers (ADMM) optimization algorithm for a transformed ℓ_1–norm minimization and used CNNs in each stage to learn the adaptive sparse representations of dynamic MRI data. The authors also proposed a novel operator referred to as soft thresholding with channel attention that learns distinct shrinkage thresholds for each feature channel. This reinforced sparsity and consequently reconstruction quality. The DUS-Net outperformed other state-of-the-art unrolled networks when evaluated using PSNR and SSIM; however, it has the highest number of parameters, which increases training cost and memory demand, making it harder for scaling to longer temporal sequences and higher resolutions.

Zhang *et al.* [28] proposed an unrolled network dubbed T^{2}LR-Net that adaptively learns the optimal transformed domain for applying tensor low–rank priors in dynamic MRI reconstruction. The approach extended the tensor Singular Value Decomposition (t-SVD) to multidimensional unitary transforms and introduced a new Unitary Transformed Tensor Nuclear Norm (UTNN). The approach overcame the limitations of a manually designed transform by using CNN modules that learn suitable transformations guided by reconstruction accuracy. The T^{2}LR – Net unrolls N iterations of the ADMM algorithm into N iteration modules, each consisting of a reconstruction block, a multiplier update block, and a transformed tensor low–rank prior block incorporated with CNN. Experimental results evaluated using SNR and SSIM showed superior results compared to other unrolling network–based methods and also optimization-based methods. However, the repeated Singular Value Decomposition (SVD) operations increase the computational complexity of the network, requiring substantial GPU memory and also training time. The Singular Value Thresholding (SVT) operators in each iteration stage might be nondifferentiable in some conditions, such as when the matrix being solved has repeated singular values, which leads to abortion of training. The performance also degrades slightly in multi-coil and prospective acquisition settings.

3. METHODOLOGY

3.1. Problem Formulation

In MRI, data is acquired using receiver coils of MR scanners with different spatial sensitivities, positioned around the patient's anatomy. The measurements are acquired in the frequency domain, commonly referred to as k-space. However, filling the entire k-space is time-consuming, so many scans are accelerated by sampling at rates below the Nyquist rate. Therefore, the main

FOREX Publication
Open Access | Rapid and quality publishing
International Journal of Electrical and Electronics Research (IJEER)
Research Article | Volume 14, Issue 2 | Pages 467-478 | e-ISSN: 2347-470X

objective of accelerated MRI reconstruction is to obtain an image from undersampled k-space data that closely resembles the ground-truth image. The reconstruction can be modelled mathematically as,

$$u = M \odot Fx + \eta \quad (1)$$

where $x \in \mathbb{C}^{N\times M}$is the target complex valued MR image of dimension $N \times M$, F is the Fourier transform operator, $u \in \mathbb{C}^{N\times M}$is the undersampled k-space data with zeros at unmeasured positions, $M \in \{0,1\}^{N\times M}$ is the binary mask indicating acquired frequency locations, $\eta \in \mathbb{C}^{N\times M}$is complex noise and $\odot$ is the Hadamard product.

Equation 1 is a purely underdetermined problem with an infinite set of solutions. According to CS theory, the reconstruction of x from y, which is an ill–posed inverse problem, involves solving the unconstrained optimization problem in *equation 2*

$$\tilde{x} = \underset{x}{argmin}\, \frac{1}{2}\|M \odot Fx - u\|_2^2 + \lambda R(x) \quad (2)$$

Where $\tilde{x}$ is the reconstructed image, $R(x)$ is the regularization term on x that encodes prior information of MR images, $\|M \odot Fx - u\|_2^2$ is the data fidelity term, $\|.\|_2^2$ denotes the ℓ_2 norm and λ is a balancing parameter.

3.2. The Learned Three-Operator Splitting Algorithm

The Three-Operator Splitting (TOS) algorithm first proposed by [29] and whose convergence analyzed in [30], and given in *algorithm 1* solves a composite optimization problem of the form;

$$\underset{x}{argmin}\ D(x) + R(x) + C(x) \quad (3)$$

where the terms D, R and C are closed, convex and proper function in smooth or non-smooth setting and D is Lipschitz differentiable.

Algorithm 1: Three operator splitting

Inputs: Initial point $y^0 \in \mathbb{C}^d$, step size γ, relaxation $\lambda > 0$

For $n = 0,1,2,\ldots. until\ convergence, N$

$x_A^n = prox_{\gamma R}(y^n)$

$z^n = 2x_A^n - y^n - \gamma \nabla D(x_A^n)$

$x_B^n = prox_{\gamma C}(z^n)$

$y^{n+1} = y^n + \lambda(x_B^n - x_A^n)$

End for

Return: x_A^N

where $prox$ is the proximal operator defined as in *equation 4* for a proper convex ϕ.

$$prox_{\gamma\phi}(x) = \underset{y\in\mathbb{C}^d}{argmin}\ \phi(y) - \frac{1}{2\gamma}\|x - y\|_2^2 \quad (4)$$

A good choice of the γ and λ ensures that the iterations converge to the minimizer of *equation 2*.

The main objective of this paper is to develop a learned reconstruction architecture that integrates the TOS iterative optimization algorithm with a data-driven prior model through algorithm unfolding. The approach efficiently and effectively addresses the challenge of solving the regularization term $R(x)$ while simultaneously alleviates the challenge of choosing the problem specific values of λ and γ. *Equation 2* can be extended to *equation 3* with $D(x)$ being the data fidelity term, $R(x)$ the regularization term and $C(x)$ enforces the complex MRI constraints by restricting the magnitude to lie within the interval [0, 1] while preserving the phase information for stability during reconstruction. Mathematically, $C(x)$ is given as,

$$C(x) = project(|x_i|, [a, b]).\, e^{j\, arg(x_i)} \quad (5)$$

where the $project$ function is defined as,

$$project(|x_i|, [a, b]) = \begin{cases} |x_i| & if\ a \le |x_i| \le b \\ a & if\ |x_i| < a \\ b & if\ |x_i| > b \end{cases} \quad (6)$$

where a and b is the magnitude range of the pixels of MR image x in this case 0 and 1 respectively, i are the location of pixels of x and $|.|$ denotes magnitude. Since computing x_A^n and choosing γ and λ efficiently and effectively is non-trival we replace the $x_A^n = prox_{\gamma R}(y^n)$ from Algorithm 1 with a parametrized Complex valued CNN (CvCNN) learned from data to form the learned TOS network (TOSNet) given in *algorithm 2*.

Algorithm 2: Learned three operator splitting network

Inputs: Zero filled image $y^0 \in \mathbb{C}^{N\times M}$, Undersampled k-space u, Binary Mask M, number of iterations N

Step size γ, relaxation λ and $\Im_{\theta_i}$are learnable parameters

For $n = 0,1,2,3\ldots N$

$x_A^n = \Im_{\theta_i}(y^n)$

$\nabla D(x_A^n) = F^{-1}\left(M \odot (Fx_A^n - u)\right)$

$z^n = 2x_A^n - y^n - \gamma \nabla D(x_A^n)$

$x_B^n = prox_{\gamma C}(z^n)$

$y^{n+1} = y^n + \lambda(x_B^n - x_A^n)$

End for

Return x_A^N

Complex-valued neural networks have several advantages over real-valued neural networks, including faster learning, easier optimization and richer representation capacity. They can preserve the phase content of MR images and hence proposed for this research. The network's neural structure uses complex-valued operations to handle complex MR data rather than splitting the imaginary and real parts into separate channels. The network structure consists of a series of N blocks corresponding to N iterations of the TOS algorithm, with the learning part comprising a Complex Valued Convolution (CVC), Complex valued Rectified Linear Unit (CReLU) and Radial Batch Normalization (RBN). The convolution operation is distributive and hence convolving the complex zero filled image $y = y_R + jy_I$ with a complex filter $f = f_R + jf_I$ becomes;

$$y * f = (f_R * y_R - f_I * y_I) + j(f_I * y_R + f_R * y_I) \quad (7)$$

where $*$ denotes convolution. In matrix notation the *equation 7* becomes;

FOREX Publication
Open Access | Rapid and quality publishing
International Journal of Electrical and Electronics Research (IJEER)
Research Article | Volume 14, Issue 2 | Pages 467-478 | e-ISSN: 2347-470X

$$\begin{bmatrix} R(f*y) \\ I(f*y) \end{bmatrix} = \begin{bmatrix} f_R & -f_I \\ f_I & f_R \end{bmatrix} * \begin{bmatrix} y_R \\ y_I \end{bmatrix} \quad (8)$$

The CvCNN uses an RBN to accelerate learning and stabilize convergence. The RBN maintains the phase information while scaling the magnitude. We first express the complex data y_{RBN} in polar form,

$$y_{RBN} = de^{j\theta} \quad (9)$$

where d is magnitude and θ is the phase. We then scale the magnitude using *equation 10;*

$$d_{RBN} = \left(\frac{d-\mu_d}{\sqrt{\sigma_d^2}}\right)\alpha + \rho + \upsilon \quad (10)$$

where σ_d^2 and μ_d are variance and mean of y_{RBN}, the constants α and ρ are trainable parameters and υ is set to 1 to ensure the normalized d_{RBN} is positive.

The real and imaginary parts are activated separately using a CReLu,

$$C\,ReLU = ReLU(y_R) + j\,ReLU(y_I) \quad (11)$$

The activation function is holomorphic when both imaginary and real components are strictly negative or positive. *Figure 1* shows a block diagram of the proposed TOSNet architecture.

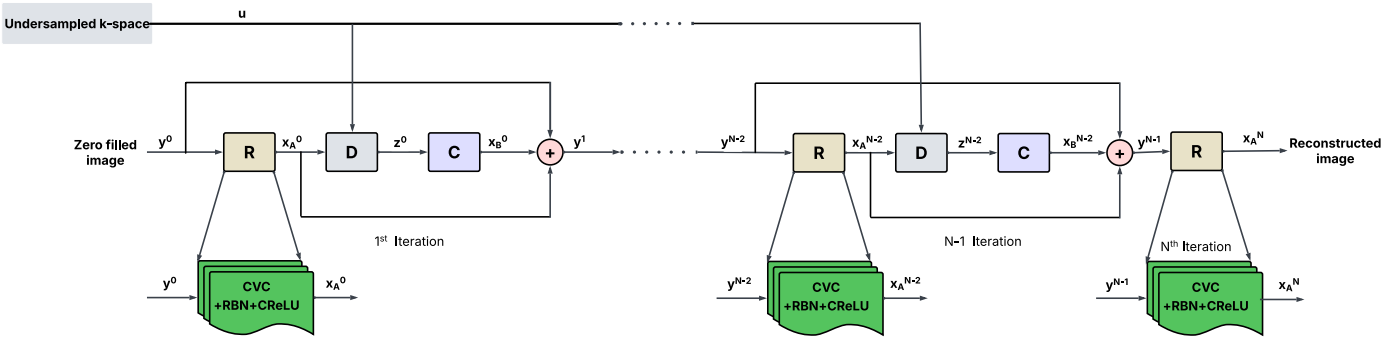

Figure 1. Block diagram of the proposed TOSNet architecture. R is the regularization block, D the data consistency block and C is the complex MRI constraints enforcement block

3.1. Loss Function

The TOSNet was trained with a linear combination of ℓ_1 and Multi-Scale SSIM (MSSIM) loss functions. The MSSIM loss function better preserves contrast and structural information in higher-frequency regions than other loss functions, such as the Mean Squared Error (MSE). Likewise, the ℓ_1 loss function preserves colour and luminance better compared to other loss functions. A linear combination of the two is achieved using *equation (12).*

$$Loss = \beta MSSIM(|x_{rec}|, |x_{tar}|) + (1-\beta)\||x_{rec}| - |x_{tar}|\|_1 \quad (12)$$

where β is an ℓ_1- MSSIM balancing weight empirically determined by [31] as 0.84, x_{rec} and x_{tar} are the reconstructed and target image respectively, $|.|$ and $|.|_1$ denote magnitude and ℓ_1 norm respectively. The MSSIM loss function is given by *equation (13).*

$$MSSIM(|x_{rec}|, |x_{tar}|) = \prod_{i=1}^{N} l_N^K(|x_{rec}|, |x_{tar}|)\, cs_i^{\nu_i}(|x_{rec}|, |x_{tar}|) \quad (13)$$

where l_N and cs_i are terms of SSIM at scale N and i defined as in *equation 14 and 15* respectively, κ and ν_i are weights of distortions factors at different resolution levels.

$$l_N(|x_{rec}|, |x_{tar}|) = \frac{2\mu_{|x_{rec}|}\mu_{|x_{tar}|} + C_1}{\mu_{|x_{rec}|}^2 + \mu_{|x_{tar}|}^2 + C_1} \quad (14)$$

$$cs(|x_{rec}|, |x_{tar}|) = \frac{2\sigma_{|x_{rec}||x_{tar}|} + C_2}{\sigma_{|x_{rec}|}^2 + \sigma_{|x_{tar}|}^2 + C_2} \quad (15)$$

Where $\mu_{|x_{rec}|}$ and $\mu_{|x_{tar}|}$ are averages of $|x_{rec}|$ and $|x_{tar}|$ respectively, $\sigma_{|x_{rec}|}$ and $\sigma_{|x_{tar}|}$ are variances of $|x_{rec}|$ and $|x_{tar}|$ respectively, C_1 and C_2 are balancing constants and $\sigma_{|x_{rec}||x_{tar}|}$ is the covariance between $|x_{rec}|$ and $|x_{tar}|$.

3.2. Implementation Details

The number of blocks for TOSNet was set to 7, a number validated through experiments and offers a good trade-off between reconstruction accuracy and computational and memory requirements. The network learning was carried out using an Adams optimizer [32] with momentum parameters set to $\beta_1 = 0.9$ and $\beta_2 = 0.999$, and a learning rate of 0.001. All the complex convolutions use a kernel size of 3×3, 5 convolutional layers and 32 hidden channels. The network was implemented using the open-source Python-based PyTorch library, with a batch size of 6. The training process was limited to 30 and 50 epochs for FastMRI and OCMR dataset respectively to ensure adequate learning while preserving generalization and preventing overfitting. The training was conducted for ×2 to ×5 acceleration in a GPU-enabled Kaggle environment using an NVIDIA Tesla P100. The CvCNN was replaced with a complex-valued Unet (CvUnet) with the same building blocks to form TOSNet$^+$.

FOREX Publication
Open Access | Rapid and quality publishing
International Journal of Electrical and Electronics Research (IJEER)
Research Article | Volume 14, Issue 2 | Pages 467-478 | e-ISSN: 2347-470X

3.3. Evaluation Metrics

The reconstruction time of the TOSNet was measured in seconds. The quality of the reconstructed MR images was assessed objectively using the SSIM, NRMSE and PSNR. The SSIM between the reconstructed and target image is given as;

$$SSIM(|x_{rec}|, |x_{tar}|) = l_N(|x_{rec}|, |x_{tar}|).\, cs(|x_{rec}|, |x_{tar}|) \quad (16)$$

where l_N and cs are defined as in *equation 14 and 15* respectively. The SSIM is a quality metric based on the human visual system that assesses image distortion in structural information. Its values lie between 0 and 1 indicating complete dissimilarity and similarity respectively. The NRMSE is given as in;

$$NRMSE(|x_{rec}|, |x_{tar}|) = \frac{\sqrt{\sum_i (|x_{rec}| - |x_{tar}|)^2}}{\sqrt{\sum_i |x_{tar}|^2}} \quad (17)$$

A low NRMSE shows good reconstruction. The PSNR of two magnitude images normalized to [0, 1] is given as;

$$PSNR(|x_{rec}|, |x_{tar}|) = -10\, log_{10}\left(\frac{1}{H \times W}\sum_i (|x_{rec}| - |x_{tar}|)^2\right) \quad (18)$$

where H and W are the height and width of the image respectively. The PSNR values range between 0 dB and $+\infty$ dB. A higher PSNR value shows higher reconstructed image quality.

4. RESULTS AND DISCUSSIONS

4.1. Datasets

The experiments were conducted on two publicly available datasets containing raw complex k-space data, namely, FastMRI [33] and the Open access multi-coil K-space dataset for Cardiovascular Magnetic Resonance imaging (OCMR) [34].

The FastMRI dataset contains both single-coil and multi-coil complex *k*-space data. The experiments were conducted using single-coil knee *k*-space data. The dataset has 973, 199 and 108 k-space volumes containing proton-density weighted images with and without fat suppression for training, validation and testing, respectively, each comprising 34,742, 7,135 and 3,903 slices, respectively. Since fat exhibits a high signal response in MRI, which hinders the clarity of details in other regions, the network was trained on volumes without fat suppression. However, some volumes without fat suppression contained incomplete or low-quality scans that provide limited anatomical information for analysis or diagnostic purposes. These volumes were removed to allow the network learn from more informative scans while also accelerating training. A total of 170, 50 and 60 volumes were selected for training, validation and testing, containing 6,150, 1,808 and 2,229 slices, respectively.

The OCMR dataset, last updated in August 2023, consists of 165 fully sampled files and 212 prospectively undersampled files collected on three Siemens MAGNETOM scanners, namely Sola (1.5T), Avanto (1.5T) and Prisma (3T). The network was trained, validated and tested using 110, 20 and 35 fully sampled files. Since the OCMR dataset provides multi-coil *k*-space data, and TOSNet was being tested on 2D MR slices with single-coil testing, we emulated single-coil data using an adaptive root-sum-of-squares with phase. The magnitude image was computed using *equation (19)*, where each coil contributes to the signal strength of the magnitude image. The phase image was obtained as a vector average of individual coil phases, as given in *equation 20*. The resulting complex-valued image was obtained by combining the phase and magnitude images as in *equation 21*.

$$|x_{tar}(i,j)| = \sqrt{\sum_k |x_k(i,j)|^2} \quad (19)$$

$$e^{j\phi_{ave}(i,j)} = \frac{\sum_k x_k(i,j)}{|\sum_k x_k(i,j)|} \quad (20)$$

$$x_{tar}(i,j) = |x_{tar}(i,j)|.\, e^{j\phi_{ave}(i,j)} \quad (21)$$

where k is the number of coils and $x_k(i,j)$is the complex image for k^{th} coil. *Figure 2* shows a sample enumerated 2D MR Cardiovascular magnitude image and its corresponding phase image.

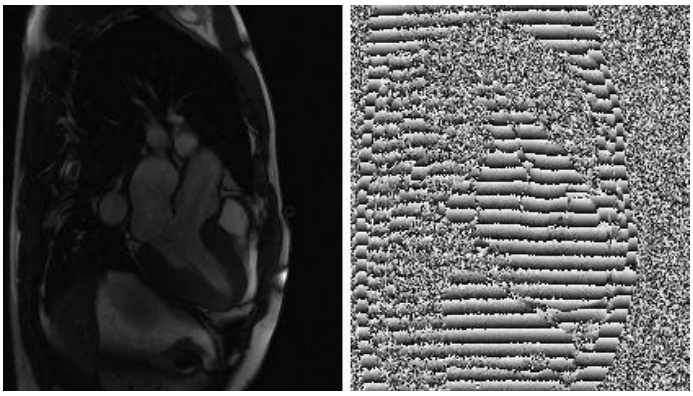

Figure 2. From left, sample enumerated magnitude image and its corresponding phase image

The enumerated images and their *k*-spaces corresponding to each file were stored in the Hierarchical Data Format version 5 (HDF5) for efficient organization and retrieval during training. A total of 2,344, 444 and 772 2D complex-valued images, along with their corresponding *k*-spaces, were obtained for training, validation and testing respectively.

4.2. Data Acquisition and Preprocessing

The number of samples acquired was reduced using a variable-density undersampling mask that mimics realistic MRI acquisition. Of the selected phase-encoding lines, 2%, 3%, 4% and 5% for ×2, ×3, ×4 and ×5 acceleration, respectively, are located at the center of k-space, corresponding to the low-frequency components that preserve the structural integrity and contrast of the reconstructed image. The remaining lines are sampled probabilistically [7] according to a smooth variable-density decay function, given in *equation 22*, ensuring denser sampling near the center and progressively sparser sampling toward the periphery. This minimizes acquisition artifacts arising from undersampling.

FOREX Publication
Open Access | Rapid and quality publishing
International Journal of Electrical and Electronics Research (IJEER)
Research Article | Volume 14, Issue 2 | Pages 467-478 | e-ISSN: 2347-470X

$$p(r) = \frac{1}{1+\left(\frac{r}{\chi}\right)^{n}} \quad (22)$$

Table 1. Objective evaluation of the number of blocks using fastMRI knee images on a ×5 acceleration

Blocks, n	Image	PSNR (dB)	SSIM	NRMSE	Time (sec/slice)
0	Zero filled	23.55	0.6307	0.0310	-
1	Reconstructed	26.78	0.7036	0.0206	0.0609
3	Reconstructed	27.31	0.7271	0.0194	0.0666
5	Reconstructed	27.95	0.7366	0.0190	0.0757
7	**Reconstructed**	**28.33**	**0.7398**	**0.0184**	**0.0860**
9	Reconstructed	28.27	0.7420	0.0183	0.0970

where n and χ were chosen empirically to be 4 and 0.4 respectively. A sample binary mask for ×2, ×3, ×4 and ×5 acceleration is showed in *figure 3* with white and black corresponding to positions of acquired and unacquired phase encoding lines respectively.

Figure 3. Sample binary mask for different accelerations

The inputs target and zero-filled image magnitude were normalized to [0, 1] while preserving the phase according to *equation 23*.

$$x_N(i,j) = \frac{x(i,j)}{max_{i,j}|x(i,j)|+\varepsilon} \quad (23)$$

where $x_N(i,j)$ is the normalized image and ε is a constant for numerical stability set to 10^{-8}. The knee images from fastMRI were center cropped to 320×320 while the Cardiovascular MR (CMR) images from OCMR dataset were zero padded if smaller and center cropped if larger to 256×256.

4.3. Determining the number of blocks *N*

The results for varying the number of TOSNet blocks using the knee images on a×5 acceleration is given in *table 1*. The performance metrics improved greatly from zero filled results which acts as baseline for comparison when learning started.

The PSNR and SSIM of the reconstructed images increase steadily as the number of blocks increases from 1 to 7 in increments of 2. Likewise, the NRMSE decreased in a similar manner. The ninth block yielded results comparable to those of the seventh block, indicating that the TOSNet had reached saturation. The average reconstruction time per slice increases steadily from 0.0609 seconds per slice with a single block and continues to rise with the addition of more blocks, even after the PSNR, SSIM and NRMSE metrics stopped showing further improvement. This led to the selection of 7 blocks for the TOSNet, which offers a good trade-off between reconstruction time and accuracy.

A sample knee image and its corresponding error map reconstructed using different number of blocks is shown in *figure 4* for subjective assessment and its performance metric given in *table 2*. The image reconstructed using a single block shows residual artifacts which diminishes with increase in the number of blocks. From block 5, the reconstructed images are visually similar to the target image. The error map, computed as the difference between the target and reconstructed image, is color-coded with blue highlighting regions of low error and bright areas indicating discrepancies between the two images. The error map for higher blocks shows lesser bright areas indicating finer reconstruction.

Table 2. Performances metric for the knee image shown in *figure 4*

Number of blocks	Image	PSNR (dB)	SSIM	NRMSE
0	Zero filled	20.23	0.6531	0.0302
1	Reconstructed	28.18	0.7730	0.0120
3	Reconstructed	29.69	0.7990	0.0101
5	Reconstructed	30.14	0.8148	0.0030
7	**Reconstructed**	**31.16**	**0.8330**	**0.0027**
9	Reconstructed	30.61	0.8238	0.0028

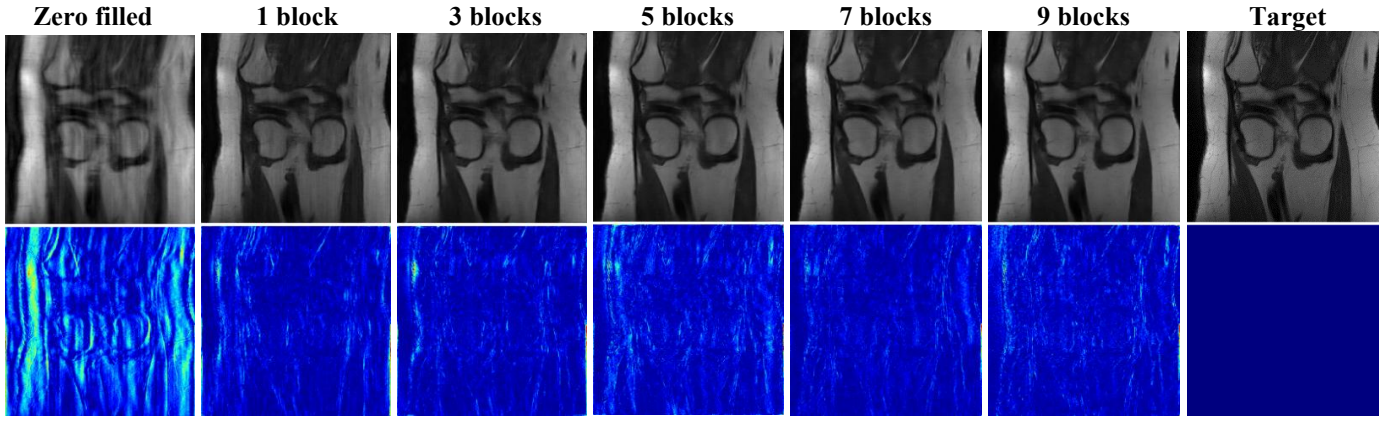

Figure 4. Sample knee image and its corresponding error map reconstructed using different number of blocks

FOREX Publication
Open Access | Rapid and quality publishing
International Journal of Electrical and Electronics Research (IJEER)
Research Article | Volume 14, Issue 2 | Pages 467-478 | e-ISSN: 2347-470X

4.4. Network Learning Characteristics

Figure 5 (a), (b), (c) and *(d)* shows the learning characteristics for TOSNet and TOSNet$^+$ under different accelerations. *Figure 1(a)* and *1(b)* shows the train loss versus the number of epochs for knee and CMR images respectively. The train loss decreases sharply for the first 15 epochs for knee images and 20 epochs for CMR images indicating fast initial learning after which the networks gradually stabilize indicating convergence. The train losses increase with increase in acceleration due to fewer samples taken for reconstruction. TOSNet$^+$ yielded lower train loss compared to TOSNet across all acceleration suggesting a better network. *Figure 5(c)* and *5(d)* shows the validation loss versus the number of epochs for knee and CMR images respectively. Similar to the train loss, the validation loss decreases sharply for the first 15 epochs for knee images and 20 epochs for CMR images indicating fast initial learning after which the networks gradually stabilize as training progresses. The validation loss increases with increase in acceleration as high undersampling results in greater loss of image information making reconstruction more challenging. The validation curves become stable after 30 epochs indicating networks convergences. The TOSNet$^+$ achieves a lower validation loss compared to TOSNet across all the accelerations indicating more accurate reconstruction.

4.5. Objective Results

Tables 3 and 4 gives the statistical reconstruction results for TOSNet and TOSNet$^+$ using the test images from FastMRI and OCMR datasets, respectively with the improvements highlighted in bold. The PSNR, SSIM and NRMSE are reported as averages computed across all test images in each dataset. The performance metrics decreased with increase in acceleration due to fewer phase encoding lines being used for reconstruction. The TOSNet$^+$ yielded higher improvements compared to TOSNet at the cost of higher reconstruction time. The average reconstruction time for TOSNet and TOSNet$^+$ is 0.0860 and 0.1393 sec/slice respectively when using knee MRI dataset and 0.0773 and 0.1185 sec/slice when using OCMR dataset. The TOSNet$^+$ has a slower reconstruction speed than TOSNet due to its more computationally expensive architecture.

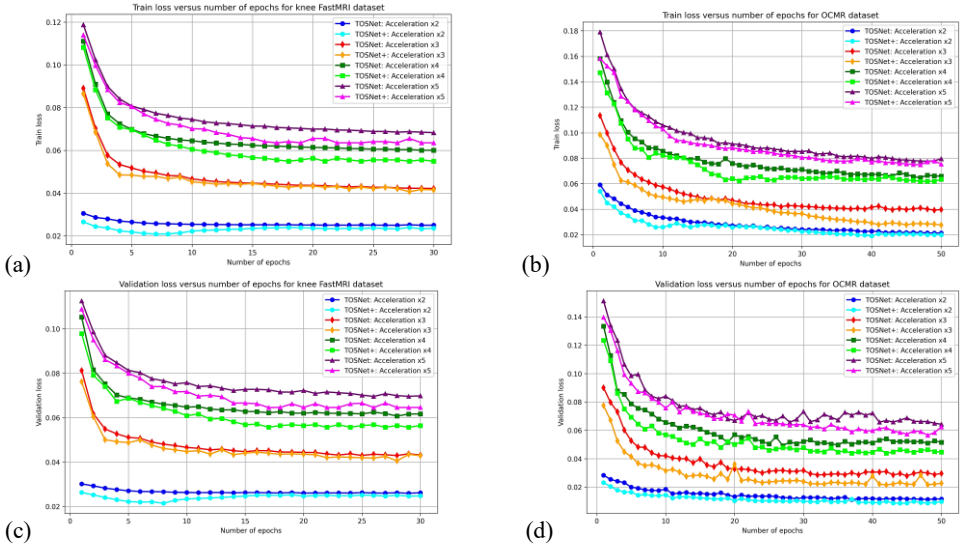

Figure 5. Networks learning characteristics

Table 3. Statistical objective results for FastMRI knee dataset. Ac denotes for acceleration

Ac	Zero filled			Reconstructed						Improvements					
				TOSNet			TOSNet$^+$			TOSNet			TOSNet$^+$		
	PSNR (dB)	SSIM	NRMSE	PSNR (dB)	SSIM	NRMSE	PSNR (dB)	SSIM	NRMSE	PSNR (dB)	SSIM	NRMSE	PSNR (dB)	SSIM	NRMSE
×2	32.06	0.8263	0.0128	33.66	0.8525	0.0112	35.26	0.8794	0.0069	**1.60**	**0.0262**	**0.0016**	**3.20**	**0.0531**	**0.0059**
×3	25.60	0.7128	0.0237	30.91	0.8078	0.0140	31.58	0.8247	0.0133	**5.31**	**0.0950**	**0.0097**	**5.98**	**0.1119**	**0.0104**
×4	23.69	0.6554	0.0298	29.05	0.7626	0.0170	29.12	0.7887	0.0165	**5.36**	**0.1072**	**0.0128**	**5.43**	**0.1333**	**0.0133**
×5	23.55	0.6307	0.0310	28.33	0.7398	0.0184	28.51	0.7560	0.0182	**4.78**	**0.1091**	**0.0126**	**4.96**	**0.1253**	**0.0128**

Table 4. Statistical objective results for OCMR dataset. Ac denotes for acceleration.

Ac	Zero Filled			Reconstructed						Improvements					
				TOSNet			TOSNet$^+$			TOSNet			TOSNet$^+$		
	PSNR (dB)	SSIM	NRMSE	PSNR (dB)	SSIM	NRMSE	PSNR (dB)	SSIM	NRMSE	PSNR (dB)	SSIM	NRMSE	PSNR (dB)	SSIM	NRMSE
×2	33.34	0.7285	0.2464	37.43	0.9550	0.1384	38.99	0.9633	0.1151	**4.09**	**0.2265**	**0.1080**	**5.65**	**0.2348**	**0.1313**
×3	26.21	0.5521	0.5094	34.73	0.9394	0.1878	36.46	0.9448	0.1526	**8.52**	**0.3873**	**0.3216**	**10.25**	**0.3927**	**0.3568**
×4	23.47	0.4884	0.6933	32.45	0.8902	0.2425	33.45	0.9198	0.2172	**8.98**	**0.4018**	**0.4508**	**9.98**	**0.4314**	**0.4761**
×5	22.39	0.4628	0.7923	31.14	0.8707	0.2819	32.20	0.8923	0.2505	**8.75**	**0.4079**	**0.5104**	**9.81**	**0.4295**	**0.5418**

FOREX Publication
Open Access | Rapid and quality publishing
International Journal of Electrical and Electronics Research (IJEER)
Research Article | Volume 14, Issue 2 | Pages 467-478 | e-ISSN: 2347-470X

4.6. Subjective Results

In this section, sample images from both FastMRI and OCMR datasets are provided for qualitative analysis. The zero filled and target images are shown alongside the reconstructed images and acts as baselines for visual comparison. The error images are also given to assist in visualizing the differences between reconstructed and target images. *Figure 6* shows sample knee MR images for visual assessment and their performance metrics given in *table 5*. The reconstructed images show great improvement from zero filled images and resemble target images. However, their differences can be seen using the error maps. The error maps of TOSNet^{+} shows fewer bright areas compared to those of TOSNet indicating finer reconstruction. The error maps of higher acceleration show more anatomical details compared to those of lower acceleration primarily due to few samples taken for reconstruction.

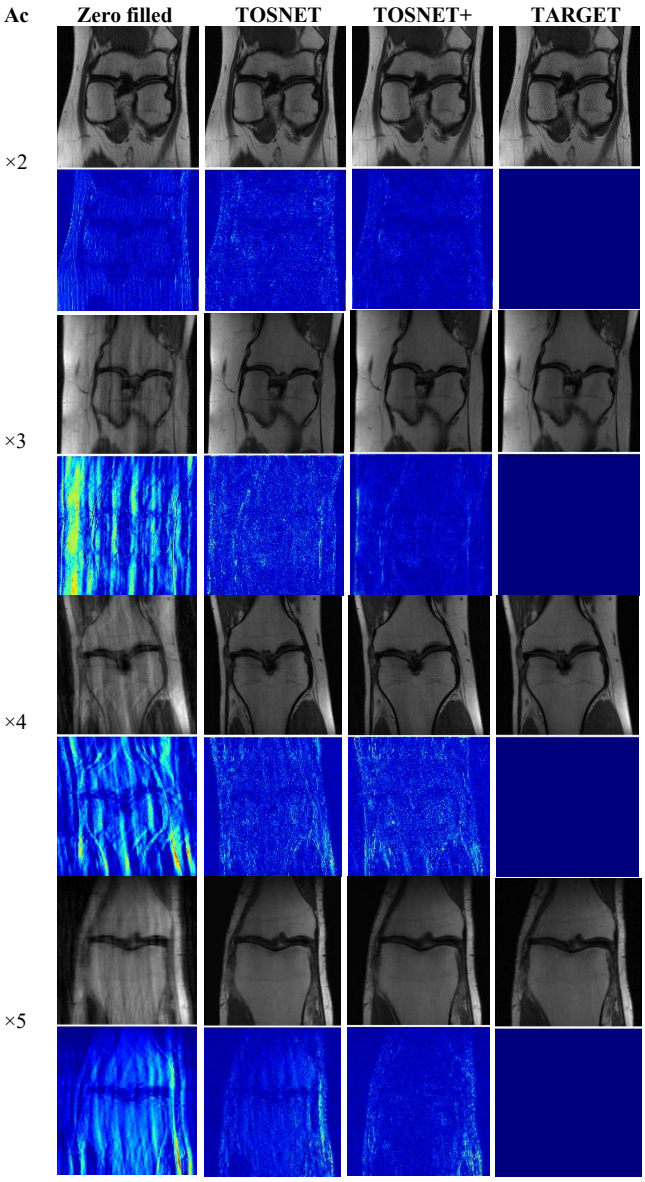

Figure 6. Sample reconstructed knee images and their corresponding error maps under different accelerations (Ac)

Figure 7 shows sample CMR images and their corresponding error maps for visual assessment. Their performance metrics is given in *table 6*. The reconstructed images show significant improvement from the zero filled images and are visually similar to the target images. The error maps of TOSNet+ shows fewer bright regions compared to TOSNet indicating better reconstruction.

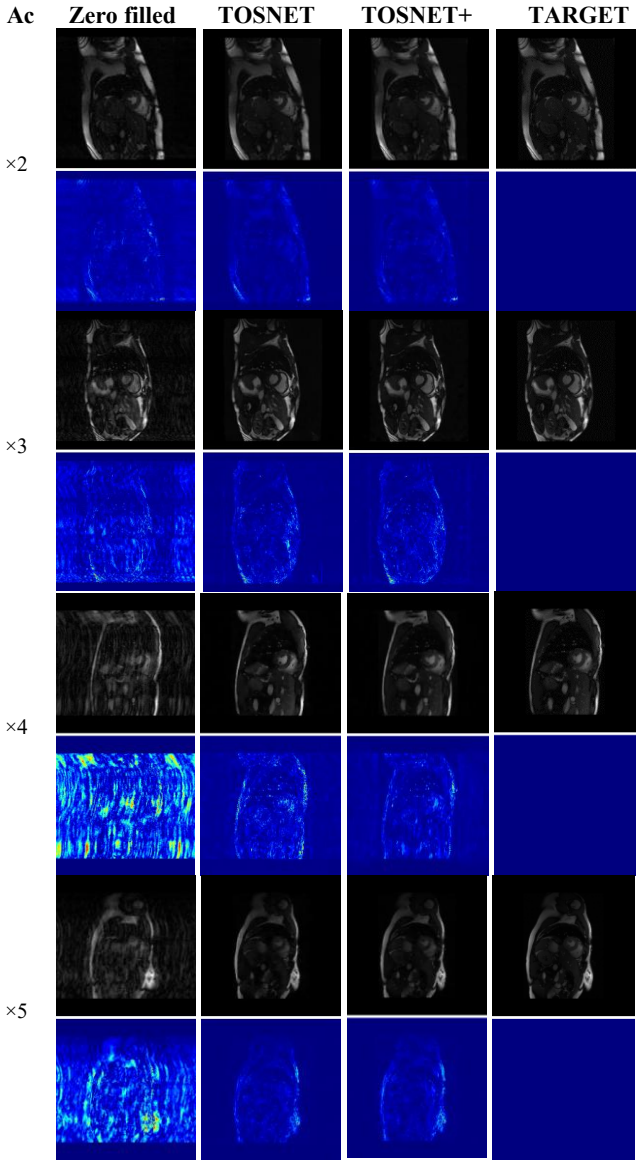

Figure 7. Sample reconstructed knee images and their corresponding error maps under different accelerations (Ac)

4.7. Comparative Methods

The proposed TOSNet and TOSNet^{+} were compared with other four state-of-the-art learned architectures, namely a Deep Cascade of Convolutional Neural Networks (DC-CNN) [35], an Interpretable Optimization-Inspired Deep Network (ISTANet) [36], Variational Network (VarNet) [37] and Learned Primal–Dual Reconstruction (LPDNet) [38]. The network architectures of the comparative methods were obtained from the authors' websites and retrained on the data used in this work for a fair

FOREX Publication
Open Access | Rapid and quality publishing
International Journal of Electrical and Electronics Research (IJEER)
Research Article | Volume 14, Issue 2 | Pages 467-478 | e-ISSN: 2347-470X

Table 5. Performances metric for the knee image shown in *figure 6*

Acceleration	Zero filled			Reconstructed					
				TOSNet			TOSNet$^+$		
	PSNR (dB)	SSIM	NRMSE	PSNR (dB)	SSIM	NRMSE	PSNR (dB)	SSIM	NRMSE
×2	30.75	0.8536	0.0028	33.74	0.8851	0.0019	36.32	0.9092	0.0015
×3	23.16	0.7666	0.0224	33.52	0.8727	0.0021	34.64	0.8777	0.0018
×4	20.28	0.6244	0.1179	31.49	0.8173	0.0102	32.34	0.8145	0.0029
×5	21.80	0.6554	0.1076	29.18	0.7852	0.0145	31.83	0.7962	0.0107

Table 6. Performances metric for the CMR images shown in *figure 7*

Acceleration	Zero filled			Reconstructed					
				TOSNet			TOSNet$^+$		
	PSNR (dB)	SSIM	NRMSE	PSNR (dB)	SSIM	NRMSE	PSNR (dB)	SSIM	NRMSE
×2	32.52	0.6953	0.0180	38.73	0.9439	0.0138	40.51	0.9676	0.0112
×3	27.59	0.5843	0.1096	37.38	0.9054	0.0168	37.96	0.9467	0.0157
×4	20.47	0.4239	0.3011	32.85	0.8408	0.0228	34.73	0.8731	0.0184
×5	23.95	0.4759	0.2174	32.78	0.9196	0.0248	33.89	0.9318	0.0219

comparison. *Table 7* presents the statistical objective results using FastMRI knee dataset for model comparison at an acceleration of ×5. The zero-filled reconstruction results are also provided and serve as a baseline for comparison with the other models' outputs. The TOSNet$^+$ yielded better results, as assessed by PSNR, SSIM and NRMSE, and consequently better MR image reconstruction than other networks. However, it has the highest average reconstruction time per slice. The TOSNet model can reconstruct images faster than the other comparative models at a comparable reconstruction quality.

Table 7. Statistical objective results of a ×5 acceleration using FastMRI knee dataset for model comparison

Method	PSNR (dB)	SSIM	NRMSE	Time (sec/slice)
Zero filled	23.55	0.6307	0.0310	-
DC-CNN	26.90	0.7124	0.0204	0.1146
ISTANet	27.0	0.7138	0.0202	0.0997
VarNet	27.69	0.7244	0.0192	0.0871
LPDNet	28.39	0.7282	0.0183	0.1188
TOSNet	28.33	0.7398	0.0184	0.0860
TOSNet$^+$	28.51	0.7560	0.0182	0.1393

A sample knee MR image reconstructed using the comparative models is shown in *figure 8* and its performance metric given in *table 8*. The target and zero-filled images are also provided and act as baselines for visual comparison. All models produced high-quality reconstruction, with anatomical structures being clearly preserved and well defined. However, the error maps can show differences in reconstruction across the comparative methods. The proposed networks exhibited the smallest reconstruction error, demonstrating their ability to preserve image fidelity and consequently superior reconstruction compared to other methods.

Table 8. Performances metric for the knee MR image shown in *figure 8* reconstructed using comparative networks

Method	PSNR (dB)	SSIM	NRMSE
Zero filled	21.40	0.6561	0.1325
DC-CNN	29.65	0.8189	0.0162
ISTANet	28.23	0.8111	0.0191
VarNet	32.13	0.8392	0.0122
LPDNet	33.08	0.8636	0.0109
TOSNet	32.37	0.8545	0.0118
TOSNet$^+$	33.40	0.8825	0.0105

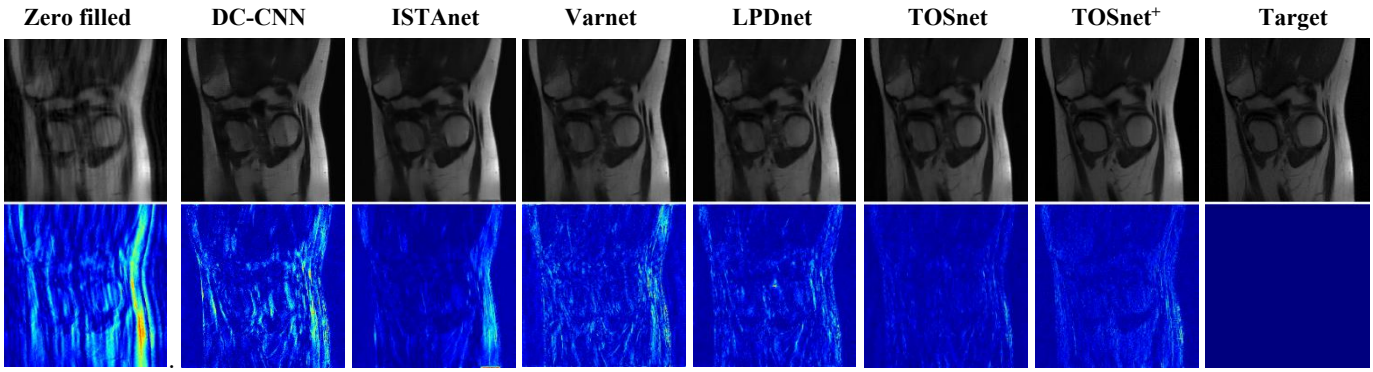

Figure 8. Sample knee image and its corresponding error map reconstructed using comparative networks

FOREX Publication
Open Access | Rapid and quality publishing
International Journal of Electrical and Electronics Research (IJEER)
Research Article | Volume 14, Issue 2 | Pages 467-478 | e-ISSN: 2347-470X

5. CONCLUSION

This paper presents a learned three-operator splitting network for accelerated MR image reconstruction. We have formulated an MRI reconstruction network inspired by the iterative procedure of the three-operator splitting method, with the regularization part replaced by a parametrized deep complex neural network to provide a richer representation of MR images, which are inherently complex. The network learns the problem-specific tuning parameters from data, thereby avoiding the need for manual selection. Each iteration is unrolled into a single network block, with the network saturating at 7 blocks, proving a good trade-off between reconstruction accuracy and computational time. Objective and subjective experimental results obtained using knee MR images from FastMRI dataset and CMR images from the OCMR dataset validates the proposed networks. The learned three-operator splitting network proposed in this work overcomes the challenges of iterative and end-to-end learning in MRI reconstruction. It shows vast potential for fast, accurate and real-time MRI, which can improve scanner performance, patient experience, and disease detection and diagnosis.

Acknowledgments: The authors are grateful to the Pan African University under the African Union Commission for the support provided throughout the research.

REFERENCES

[1] Y. Lian, Z. Liu, J. Wang, and S. Lu, "Spatial-frequency aware zero-centric residual unfolding network for MRI reconstruction," *Magnetic Resonance Imaging,* vol. 117, pp. 110334, Jan. 2025, doi:10.1016/j.mri.2025.110334.

[2] W. Bian and Y. K. Tamilselvam, "A review of Optimization-Based Deep Learning Models for MRI Reconstruction," *AppliedMath*, vol. 4, no. 3, pp. 1098–1127, Sep. 2024, doi: 10.3390/appliedmath4030059.

[3] Y. Zhang, H. Gui, N. Yang, and Y. Hu, "JotlasNet: Joint tensor low-rank and attention-based sparse unrolling network for accelerating dynamic MRI," *Magnetic Resonance Imaging,* vol. 118, pp. 110337, Jan. 2025, doi: 10.1016/j.mri.2025.110337.

[4] B. Vasudeva, P. Deora, S. Bhattacharya, and P. M. Pradhan, "Compressed Sensing MRI Reconstruction with Co-VeGAN: Complex-Valued Generative Adversarial Network," *2022 IEEE/CVF Winter Conference on Applications of Computer Vision (WACV)*, pp. 1779–1788, Jan. 2022, doi: 10.1109/wacv51458.2022.00184.

[5] M. I. Doneva, M. Akcakaya, and C. Prieto, *Magnetic resonance image reconstruction: Theory, Methods and Applications*. Academic Press,2022.

[6] D. L. Donoho, "Compressed sensing," *IEEE Transactions on Information Theory*, vol. 52, pp. 1289–1306, Apr. 2006, doi: 10.1109/tit.2006.871582.

[7] M. Lustig, D. Donoho, and J. M. Pauly, "Sparse MRI: The application of compressed sensing for rapid MR imaging," *Magnetic Resonance in Medicine*, vol. 58, pp. 1182–1195, Oct. 2007, doi: 10.1002/mrm.21391.

[8] S. Ma, W. Yin, Y. Zhang and A. Chakraborty, "An efficient algorithm for compressed MR imaging using total variation and wavelets," *2008 IEEE Conference on Computer Vision and Pattern Recognition*, Anchorage, AK, USA, 2008, pp. 1-8, doi: 10.1109/CVPR.2008.4587391.

[9] J. C. Ye, "Compressed sensing MRI: a review from signal processing perspective," *BMC Biomedical Engineering*, vol. 1, no. 1, pp. 8, Mar. 2019, doi: 10.1186/s42490-019-0006-z.

[10] N. Fuin, A Bustin, T Küstner et al., "A multi-scale variational neural network for accelerating motion-compensated whole-heart 3D coronary MR angiography," *Magnetic Resonance Imaging,* vol. 70, pp. 155–167, Apr. 2020, doi: 10.1016/j.mri.2020.04.007.

[11] Md. B. Hossain, R. K. Shinde, S. Oh, K.-C. Kwon, and N. Kim, "A systematic review and identification of the challenges of deep learning techniques for undersampled magnetic resonance image reconstruction," *Sensors,* vol. 24, no. 3, pp. 753, Jan. 2024, doi: 10.3390/s24030753.

[12] S. Kiryu, H. Akai, K. Yasaka *et al.*, "Clinical impact of deep learning reconstruction in MRI," *Radiographics*, vol. 43, no. 6, pp. e220133, May 2023, doi: 10.1148/rg.220133.

[13] P. Guo, Y. Mei, J. Zhou, S. Jiang, and V. M. Patel, "ReconFormer: Accelerated MRI Reconstruction using Recurrent Transformer," *IEEE Transactions on Medical Imaging*, vol. 43, no. 1, pp. 582–593, Sep. 2023, doi: 10.1109/tmi.2023.3314747.

[14] X. Zhao, T. Yang, B. Li, and X. Zhang, "SwinGAN: A dual-domain Swin Transformer-based generative adversarial network for MRI reconstruction," *Computers in Biology and Medicine*, vol. 153, Dec. 2022, doi: 10.1016/j.compbiomed.2022.106513.

[15] G. Ongie, A. Jalal, C. A. Metzler, R. G. Baraniuk, A. G. Dimakis, and R. Willett, "Deep learning techniques for inverse problems in imaging," *IEEE Journal on Selected Areas in Information Theory*, vol. 1, no. 1, pp. 39–56, May 2020, doi: 10.1109/jsait.2020.2991563.

[16] G. Yang, S. Yu, H. Dong *et al.*, "DAGAN: Deep De-Aliasing Generative Adversarial Networks for Fast Compressed Sensing MRI Reconstruction," *IEEE Transactions on Medical Imaging*, vol. 37, no. 6, pp. 1310–1321, Dec. 2017, doi: 10.1109/tmi.2017.2785879.

[17] Y. Han, L. Sunwoo, and J. C. Ye, K -Space Deep Learning for Accelerated MRI," *IEEE Transactions on Medical Imaging*, vol. 39, no. 2, pp. 377–386, Jul. 2019, doi: 10.1109/tmi.2019.2927101.

[18] Y. Yang, J. Sun, H. Li and Z. Xu. ADMM-Net: a deep learning approach for compressive sensing MRI. In: *Advances in neural information processing systems;* 2017. pp. 10–8.

[19] C. Qin, J. Schlemper, J. Caballero, A. N. Price, J. V. Hajnal, and D. Rueckert, "Convolutional recurrent neural networks for dynamic MR image reconstruction," *IEEE Transactions on Medical Imaging*, vol. 38, no. 1, pp. 280–290, Aug. 2018, doi: 10.1109/tmi.2018.2863670.

[20] H. K. Aggarwal, M. P. Mani, and M. Jacob, "MODL: Model-Based Deep Learning Architecture for Inverse Problems," *IEEE Transactions on Medical Imaging*, vol. 38, no. 2, pp. 394–405, Aug. 2018, doi: 10.1109/tmi.2018.2865356.

[21] C. M. Sandino, P. Lai, SS. Vasanawala, JY Cheng. Accelerating cardiac cine MRI using a deep learning-based ESPIRiT reconstruction. *Magnetic Resonance in Medicine*, 2020, doi:10.1002/mrm.28420.

[22] Y. Zhang, X. Li, W. Li, and Y. Hu, "Deep unrolling shrinkage network for dynamic MR imaging," *2023 IEEE International Conference on Image Processing (ICIP)*, pp. 1145–1149, Sep. 2023, doi: 10.1109/icip49359.2023.10223077.

[23] M. Vornehm, J. Wetzl, D. Giese *et al.*, "CineVN: Variational network reconstruction for rapid functional cardiac cine MRI," *Magnetic Resonance in Medicine*, vol. 93, no. 1, pp. 138–150, Aug. 2024, doi: 10.1002/mrm.30260.

[24] J. Schlemper, J. Caballero, J. V. Hajnal, A. N. Price, and D. Rueckert, "A deep cascade of convolutional neural networks for dynamic MR image reconstruction," *IEEE Transactions on Medical Imaging*, vol. 37, no. 2, pp. 491–503, Feb. 2018, doi: 10.1109/tmi.2017.2760978.

[25] J. Duan, J. Schlemper, C. Qin *et al.*, "VS-Net: Variable splitting network for accelerated parallel MRI reconstruction," *arXiv (Cornell University)*, Jan. 2019, doi: 10.48550/arxiv.1907.10033.

[26] B. Xin, TS Phan, L Axel, et al. Learned half-quadratic splitting network for magnetic resonance image reconstruction. arXiv 2021.

[27] Z. Fabian, B Tinaz, M Soltanolkotabi, "HUMUS-net: hybrid unrolled multi-scale network architecture for accelerated MRI reconstruction" *Adv Neural Inf Process Syst,* 2022;35:25306–19.

[28] Y. Zhang, P. Li, and Y. Hu, "T2LR-Net: An unrolling network learning transformed tensor low-rank prior for dynamic MR image reconstruction," *Computers in Biology and Medicine*, vol. 170, pp. 108034, Jan. 2024, doi: 10.1016/j.compbiomed.2024.108034.

[29] D. Davis and W. Yin, "A Three-Operator Splitting Scheme and its Optimization Applications," *Set-Valued and Variational Analysis*, vol. 25, no. 4, pp. 829–858, Jun. 2017, doi: 10.1007/s11228-017-0421-z

International Journal of
Electrical and Electronics Research (IJEER)
Research Article | Volume 14, Issue 2 | Pages 467-478 | e-ISSN: 2347-470X

[30] H. Wang, M. Fazlyab, S. Chen, and V. M. Preciado, Eds. Robust Convergence Analysis of Three-Operator Splitting, *2019 57th Annual Allerton Conference on Communication, Control, and Computing (Allerton)*. IEEE, 2019. doi: 10.1109/ALLERTON.2019.8919695

[31] H. Zhao, O. Gallo, I. Frosio, and J. Kautz, "Loss functions for image restoration with neural networks," *IEEE Transactions on Computational Imaging*, vol. 3, pp. 47–57, Dec. 2016, doi: 10.1109/tci.2016.2644865.

[32] D.P. Kingma and J.L. Ba, "Adam: A Method for Stochastic Optimization," *International Conference on Learning Representations (ICLR),* Dec 2014.

[33] J. Zbontar, F. Knoll, A. Sriram *et al.*, "FastMRI: an open dataset and benchmarks for Accelerated MRI," *arXiv (Cornell University)*, Jan. 2018, doi: 10.48550/arxiv.1811.08839.

[34] C. Chen, Y. Liu, P. Schniter *et al.*, "OCMR (V1.0) --Open-Access Multi-Coil K-Space Dataset for Cardiovascular Magnetic Resonance Imaging," *arXiv (Cornell University)*, Jan. 2020, doi: 10.48550/arxiv.2008.03410.

[35] J. Schlemper, J. Caballero, J. V. Hajnal, A. N. Price, and D. Rueckert, "A deep cascade of convolutional neural networks for dynamic MR image reconstruction," *IEEE Transactions on Medical Imaging*, vol. 37, no. 2, pp. 491–503, Oct. 2017.

[36] J. Zhang and B. Ghanem, "ISTA-Net: Interpretable Optimization-Inspired Deep Network for Image Compressive Sensing," *2018 IEEE/CVF Conference on Computer Vision and Pattern Recognition*, Salt Lake City, UT, USA, 2018, pp. 1828-1837, doi: 10.1109/CVPR.2018.00196.

[37] K. Hammernik, T. Klatzer, E. Kobler, M. P. Recht, D. K. Sodickson, T. Pock, and F. Knoll, "Learning a variational network for reconstruction of accelerated MRI data," *Magnetic Resonance in Medicine*, vol. 79, no. 6, pp. 3055–3071, Nov. 2017.

[38] J. Adler and O. Oktem, "Learned Primal-Dual reconstruction," IEEE Transactions on Medical Imaging, vol. 37, no. 6, pp. 1322–1332, Jan. 2018, doi: 10.1109/tmi.2018.2799231.